BJR https://doi.org/10.1259/bjr.20220059

Received: 11 January 2022 | Accepted: 12 May 2022 | Published online: 10 June 2022

Cite this article as:
Wiesinger F, Ho M-L. Zero-TE MRI: principles and applications in the head and neck. *Br J Radiol* (2022) 10.1259/bjr.20220059.

REVIEW ARTICLE

Zero-TE MRI: principles and applications in the head and neck

[1,2]FLORIAN WIESINGER, PhD and [3]MAI-LAN HO, MD

[1]Department for Neuroimaging, Institute of Psychiatry & Neuroscience, King's College London, London, UK
[2]Principal Scientist at GE Healthcare, Munich, Germany
[3]Nationwide Children's Hospital and The Ohio State University, Columbus, USA

Address correspondence to: Dr Mai-Lan Ho
E-mail: *ho.538@osu.edu*

ABSTRACT

Zero echo-time (ZTE) MRI is a novel imaging technique that utilizes ultrafast readouts to capture signal from short-T2 tissues. Additional sequence advantages include rapid imaging times, silent scanning, and artifact resistance. A robust application of this technology is imaging of cortical bone without the use of ionizing radiation, thus representing a viable alternative to CT for both rapid screening and "one-stop-shop" MRI. Although ZTE is increasingly used in musculoskeletal and body imaging, neuroimaging applications have historically been limited by complex anatomy and pathology. In this article, we review the imaging physics of ZTE including pulse sequence options, practical limitations, and image reconstruction. We then discuss optimization of settings for ZTE bone neuroimaging including acquisition, processing, segmentation, synthetic CT generation, and artifacts. Finally, we examine clinical utility of ZTE in the head and neck with imaging examples including malformations, trauma, tumors, and interventional procedures.

INTRODUCTION

Zero echo-time (ZTE) MRI is a novel imaging technique that utilizes ultrafast readouts to capture signal from short-T2 tissues. Additional sequence advantages include rapid examination times, silent scanning, and artifact resistance. One robust application of this technology is imaging of cortical bone without ionizing radiation, which represents a viable alternative to CT for both rapid screening and "one-stop-shop" MRI. Although ZTE is increasingly used in musculoskeletal and body imaging, neuroimaging applications have been limited by the complex anatomy and pathology of the head and neck. In this article, we review the imaging physics of ZTE including pulse sequence options, practical limitations, and image reconstruction. We then discuss optimization of settings for bone imaging including acquisition, processing, segmentation, synthetic CT generation, and artifacts. Finally, we examine clinical utility in the head and neck with imaging examples including craniofacial malformations, trauma, chronic disorders, and interventional procedures.

ZTE IMAGING PHYSICS

ZTE is an MRI pulse sequence based on non-selective volume excitation and 3D radial center-out k-space encoding.[1] Distinct from conventional MRI pulse sequences, ZTE uses a readout gradient amplitude that is kept constant throughout the scanning with only small directional updates in between repetitions. This approach yields unique properties in terms of silent scanning and nominal zero echo time (*i.e.* TE = 0). Like ultrashort TE (UTE) imaging, ZTE acquires free induction decay (FID) signal that does not rely on gradient echo or spin echo signal refocusing. The term ZTE was coined by Weiger et al,[2] and refers to a method invented and pioneered by Madio and Lowe in the 1990s that was originally known as RUFIS (Rotating Ultra-Fast Imaging Sequence).[1] In this manuscript, we will summarize ZTE characteristics with respect to the pulse sequence, image reconstruction and contrast behavior, including specific considerations such as dead-time gap and flip angle limitations. For educational purposes, we will refer to a typical ZTE experiment with imaging bandwidth BW_{RX} = 62.5 kHz and 3D isotropic image matrix of $Nmtx^3 = 256^3$ points. For more in-depth discussion of ZTE physics, we refer the interested reader to excellent reviews by Weiger et al[2,3] and Ljungberg et al.[4] Table 1 provides an overview of the major physics considerations in ZTE.

Native pulse sequence

Among the vast array of existing MR pulse sequences, ZTE is arguably one of the simplest in terms of radiofrequency

Table 1. Major physics considerations in ZTE

Characteristic	Description
Pulse sequence	Constant readout gradient amplitude in combination with short block-pulse RF excitation enables nominal TE = 0 acquisition with 3D center-out radial k-space sampling. These characteristics permit rapid, silent, and artifact-resistant imaging of short-T2 tissues.
Flip angle	Limited to maximum of ~4° in conventional MR imaging systems, in order for RF block pulses to achieve consistent excitation independent of the readout gradient.
Image encoding	3D straight, center-out, radial spokes are scanned sequentially in a smooth spiral trajectory along the surface of spherical k-space. Enforcing Nyquist sampling at the edge of k-space requires a total of $p^*N_{mtx}^2$ radial spokes, with p-fold undersampling resulting in $N_{spk} = N_{mtx}^2$ of required spokes.
Image reconstruction	Non-Cartesian radial sampling requires 3D gridding image reconstruction. Advanced reconstruction methods include parallel imaging, total generalized variation regularization, compressed sensing, and deep learning.
Steady-state response	Exceptionally short TR is primarily determined by the readout duration T_{read}. Compared to conventional pulse sequences, additional factors are of negligible duration. The steady-state signal response is of T1 and PD-weighted spoiled-gradient echo nature, with signal spoiling achieved via RF spoiling and the readout gradient.
Image contrast	Magnetization-prepared ZTE has been implemented for a wide range of image contrasts including T1, T2, ASL-based MR angiography, magnetization transfer, diffusion, and quantitative parametric mapping. ZTE can be turned into a multiecho sequence via gradient refocusing, followed by equidistant gradient echoes that provide additional T2* information.
Dead-time gap	Sampling the FID can begin only after RF hardware changes state from transmit to receive. This gap time is termed the transmit-receive switching time, dt_{TxRx}, and ranges from ~8 to 100 ms on conventional MRI systems. This center k-space gap can be addressed with minimal impact on scan time via algebraic image reconstruction, and/or single-point imaging, reacquisition of the gradient scaled original ZTE scan.

FID, free induction decay; PD, proton density; RF, radiofrequency; TE, echo time; TR, repetition time; ZTE, zero echo-time.

(RF) and gradient waveform complexity. Conceptually, ZTE is based on the RUFIS pulse sequence,[1] consisting of a constant readout gradient amplitude (not ramped down or up between repetitions) in combination with short block-pulse RF excitation. With the readout gradient kept constant, spatial signal encoding starts immediately at the time of RF excitation, resulting in nominal zero echo time (TE = 0) FID acquisition. This allows for capture of short-lived MRI signals from short-T2 tissues such as cortical bone. The direction (but not amplitude) of the x, y, z readout gradient is updated in between repetitions, resulting in 3D center-out radial k-space sampling. By arranging the 3D radial spokes such that their end points follow a smooth spiral trajectory along the surface of the 3D spherical k-space, gradient switching can be reduced to an inaudible level and enables silent imaging.[5] Furthermore, this method also provides exceptionally short repetition times (TR) and resistance to MRI artifacts, such as eddy currents and motion. For the considered ZTE example with BW_{Rx} = 62.5 kHz (corresponding to a sampling time of Dt_{Rx} = $1/BW_{Rx}$ = 16 ms) and image matrix of $N_{mtx} = 256^3$, the number of center-out readout points is $N_{read} = 256/2 = 128$, which results in an ultrafast readout of $T_{read} = N_{read}{}^*Dt_{Rx} = 128^*16ms$ = 2.048 ms (Figure 1),

Flip angle limitations

Unlike conventional MR pulse sequences, in ZTE the RF excitation is entangled with the image encoding readout gradient.[6–9] In order for the RF block pulses to achieve consistent excitation independent of the readout gradient, the RF excitation bandwidth has to encompass the full RF imaging bandwidth (*i.e.* $BW_{Tx} \geq BW_{Rx}$). This means that the RF pulse width must be shorter than the RF sampling time (*i.e.* $Dt_{Tx} \leq Dt_{Rx}$), which in turn limits the maximum achievable flip angle. Otherwise, the readout gradient would result in a sinc-shape modulation of the RF excitation profile along the readout direction. Since the readout changes direction over the course of the sequence, this would result in blurring that scales with increasing distance from the center of the imaging field of view (FOV). For the considered ZTE example with BW_{Rx} = 62.5 kHz (and $Dt_{Rx} = 1/BW_{Rx}$ = 16 ms), this limits the pulse width of the RF excitation block pulse to very short durations of $Dt_{Rx} \leq 16$ ms, corresponding to a maximum flip angle of only ~4° assuming a maximum RF amplitude of $B_{1,max}$ = 16 mT (typical for whole-body human MRI systems). Using longer RF excitation pulses (*i.e.* $Dt_{Tx} \geq Dt_{Rx}$) would result in image blurring, especially towards the edge of the imaging FOV.[6,9] Recently, Froidevaux et al developed pulse encoding for ZTE imaging that enables higher flip angle excitations by extending the RF pulse duration.[10]

Image encoding and reconstruction

ZTE samples 3D k-space along straight, center-out, radial spokes that are scanned sequentially, such that their end points follow a smooth spiral trajectory along the surface of the spherical k-space. With equidistant spacing of samples acquired along each 3D center-out radial spoke, the resultant angular sampling is very high in the k-space center and lower toward the periphery. Enforcing Nyquist sampling at the edge of the k-space requires a total of $p^*N_{mtx}^2$ radial spokes. Practically, p-fold undersampling is considered acceptable and results in $N_{spk} = N_{mtx}^2$ of required spokes. Higher undersampling factors would result in streaking, a characteristic artifact for 3D radial scanning. Hence, for the considered ZTE example with N_{mtx} = 256, a total of $N_{spk} = 256^2$=65,536 spokes are required.

The non-Cartesian radial sampling requires 3D gridding image reconstruction.[11–13] Advanced methods such as parallel imaging,[14] total generalized variation (TGV) regularization,[15]

Figure 1. Schematic of the ZTE pulse sequence showing RF and gradient waveforms (left) and corresponding 3D radial center-out k-space sampling (right). For illustrative purposes, the RF pulse width is extended and a very small number of spokes (N_{spk} = 1024) are considered. ZTE, zero echo-time; RF, radiofrequency.

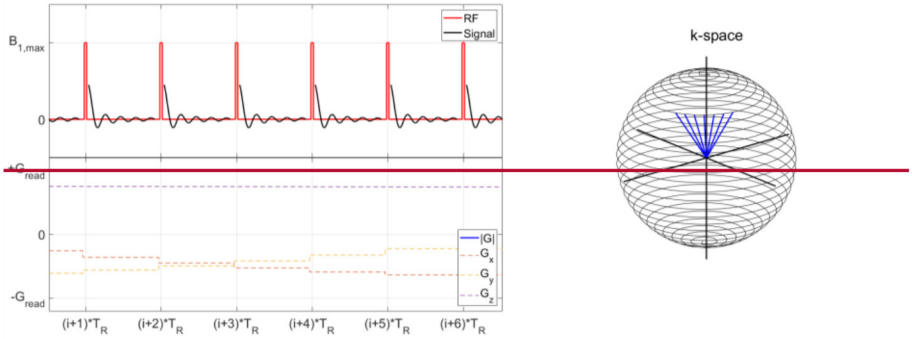

and compressed sensing[16] are available for ZTE via the open-source RIESLING image reconstruction toolbox.[17] Recently, a novel deep learning (DL)-based image reconstruction method[18] has been applied to ZTE for significant reduction in scan times and/or improved image quality.[19]

Steady-state signal response

ZTE imaging allows rapid scanning with exceptionally short repetition times (TRs), which are primarily determined by the readout duration (T_{read}). Additional factors, such as RF pulse duration and gradient update time, are of negligible duration in comparison to T_{read}. Compared to conventional MRI pulse sequences, ZTE does not involve delays due to slice-rewinding, phase-encoding, frequency pre-winding, or gradient spoiling. For the considered ZTE example (*i.e.* BW_{Rx} = 62.5 kHz, N_{mtx} = 128), the repetition time TR ~2 ms. This results in a total scan time of N_{spk}*TR = 65536*2ms = 131 s, without acceleration techniques such as parallel imaging or compressed sensing.

The steady-state signal response of the ZTE pulse sequence is of a T1 and proton density (PD)-weighted spoiled-gradient echo (SPGR) nature, with signal spoiling achieved via RF spoiling and the readout gradient. More concretely, for zero nominal TE (*i.e.* TE = 0), small flip angle (*i.e.* α << 90°) and short TR (*i.e.* TR<<T1), the steady-state longitudinal magnetization ($M_{z,ss}$) can be stated as[4,9]:

$$M_{z,SS} = \frac{PD.(1-E_1).E_2^*}{(1-E_1.\cos\alpha)} \cong \frac{PD}{1+\frac{T1}{TR}\frac{\alpha^2}{2}},\ with\ E_1 = e^{-\frac{TR}{T1}},\ and\ E_2^* = e^{-\frac{T_2^*}{TE}} \quad [1]$$

with PD the proton density, T1 the longitudinal relaxation time, and T2* the effective transverse relaxation time. The corresponding signal to noise (SNR)-optimal Ernst (α_{Ernst}) can then be stated as:

$$\alpha_{Ernst} = \text{acos}\left(E_1\right) \cong \sqrt{\frac{2.T1}{TR}} \quad [2]$$

Equation [1] demonstrates the ability of ZTE for rapid and silent 3D PD and T_1 weighted SGPR-type imaging with TE = 0. Because of the very short repetition times, the Ernst flip angle (α_{Ernst}) is also small and within the flip angle limitation discussed above. In our example, with longitudinal relaxation time of T1 = 1 s and TR = 2 ms, the Ernst flip angle becomes α_{Ernst} ~ 3.6°. With careful parameter adjustment, ZTE also allows variable flip angle PD and T1 mapping[9] similar to DESPOT.

Magnetization preparation and multigradient echo

Magnetization preparation in combination with segmented readout is a flexible and powerful concept for contrast enhancement of otherwise contrast-limited pulse sequences.[20] The best-known example is MP-RAGE,[21] which is based on inversion-recovery T1 preparation followed by segmented gradient echo (GRE) acquisition. The intrinsic characteristics of ZTE (rapid, silent, 3D image encoding with very short TR and TE = 0) are well suited for combination with magnetization preparation. Magnetization prepared ZTE has been implemented for a wide range of image contrasts including T1,[5,9], T2,[22] ASL-based MR angiography (MRA),[23] magnetization transfer (MT),[24] diffusion,[25] and quantitative parametric mapping.[19]

Analogous to multiecho GRE or UTE, ZTE can be turned into a multiecho sequence via gradient refocusing to acquire the original FID, followed by equidistant gradient echoes that provide additional T2* information. Multiecho ZTE has been used to generate positive bone contrast by subtracting a later in-phase gradient-echo from the TE = 0 FID image.[26] Using conventional bipolar gradients results in loud acoustic noise. Quiet ZTE-based multigradient echo imaging can be achieved using the Looping Star sequence[27] where multiple FID signals are first excited and then sequentially gradient refocused in a looping, time-multiplexed manner.

Dead-time gap

Even though ZTE starts image encoding immediately at the time of RF excitation, the MR system can start sampling the FID signal only after RF hardware changes state from transmit to receive. This gap time is termed the transmit-receive switching

Table 2. ZTE characteristics pertinent to bone neuroimaging

Characteristic	Explanation
High bandwidth imaging	Rapid scanning and efficient capture of short-lived bone signal with minimal T2 decay. Limited flip angle yields proton density-weighted images with uniform bone appearance and low-contrast soft tissue.
Bone enhancement	Bias correction, intensity normalization, and inverse linear scaling produce standardized signal response across the imaging field-of-view.
Bone segmentation	In a typical histogram distribution of ZTE signal, there are clear peaks for air and soft tissue, with an intervening broader bone peak. Air, tissue, and bone segmentations can be obtained via intensity thresholding and morphologic operations to account for partial volume effects.
Synthetic CT	Point-based operations (intensity thresholding and linear scaling) have been used to generate synthetic CT images for adult subjects with relatively normal bone anatomy. This can be used for basic applications such as MR-only radiation treatment planning and PET/MR attenuation correction. For more complex head and neck pathologies (poorly mineralized, thin, or irregular bone and variable soft tissues), DL-powered synthetic CT approaches show promise but are not fully optimized for anatomic delineation.
Chemical shift artifacts	Due to 3D radial sampling, ZTE image quality can be severely affected by fat-water off-resonance. Chemical shift artifacts manifest with image blurring and signal interference at fat-water interfaces, which degrades the clarity of cortical bone depiction. These artifacts can be minimized by changing imaging parameters (increasing bandwidth, coarser spatial resolution, decreasing B_0 field strength), and/or performing chemical shift decomposition-based in-phase reconstruction.
Alternative techniques	Other options for bone imaging include UTE and GRE, which involve longer imaging times with darker and more pronounced bone signal due to additional susceptibility effects. However, this decreases the ability to distinguish cortical bone from medullary bone and other short-T2 tissues.

GRE, gradient echo time; PET, positron emission tomography; UTE, ultrashort echo time; ZTE, zero echo-time.

time, dt_{TxRx}. Depending on the RF coil and system characteristics, dt_{TxRx} ranges from ~8 to 100 ms. Because of this finite transmit-receive switching delay, the first few data samples of the center-out 3D radial spokes are missed resulting in a spherical gap of samples at the center of k-space. Continuing with our example (*i.e.* BW_{RX} = 62.5 kHz, Dt_{Rx} = 16 ms) and assuming a transmit-receive switching time of dt_{TxRx} = 32 ms results in a spherical gap of five samples' diameter. This center k-space gap can be addressed with minimal impact on scan time via algebraic image reconstruction[28] or collection of the missed k-space samples using either single-point imaging,[29] reacquisition of the gradient scaled original ZTE scan,[30] or a combination thereof.[31]

ZTE for bone neuroimaging

MRI is well established for superior soft tissue contrast and multiple sequence weightings, but has not historically been utilized for structural bone assessment. This is because cortical bone is an extremely dry tissue with low proton density (~20% water) and short signal lifetimes (T2 ~390 ms at 3 T).[32] Conventional MRI gradient echo or spin echo sequences with TEs in the millisecond range are generally too slow for meaningful bone signal detection. The following section explains ZTE bone imaging via PD-weighted ZTE and contrast-inversion as originally described by Wiesinger et al.[33,34] Table 2 summarizes ZTE characteristics pertinent to bone neuroimaging.

High bandwidth PD-weighting

ZTE bone imaging exploits the natural strength of ZTE for high bandwidth, PD-weighted MRI.[33] More specifically, the zero echo time (TE = 0) characteristic in combination with high bandwidth imaging (*i.e.* fast sampling) assures rapid scanning and efficient capture of short-lived MRI bone signals with minimal T2 signal decay. High imaging bandwidth in turn limits the flip angle, leading to the desired PD-weighted contrast with minimal T1 saturation,[1] producing a uniform bone appearance with low-contrast soft tissue. In essence, high bandwidth PD-weighted ZTE enables excellent bone imaging by: (1) efficiently capturing weak short-lived MRI bone signals and (2) contrasting them against surrounding soft tissue and air. DL-based image reconstruction can further reduce noise and improve ringing artifacts. We show an example case (1.5 T, BW = 125 kHz, FA = 1°, FOV = 300×300 x 200 mm^3, res = 1×1 x 1 mm^3, 2 min 1 s scan time) using standard gridding (first row) and DL-based image reconstruction[18,19] with 75% denoising and 75% de-ringing (second row). A point-based synthetic CT reconstruction is demonstrated with logarithmic inversion of the grayscale (third row) to suppress soft tissue and enhance bone (Figure 2).

Image processing for bone enhancement

To enhance bone depiction, PD-weighted ZTE images undergo several image processing steps including bias correction, intensity normalization, and inverse linear scaling.[33,34] Bias correction eliminates smooth spatial signal intensity variations originating from the RF excitation and signal reception. This includes measured coil sensitivity maps obtained from dedicated fast calibration scans (similar to those used in parallel imaging) and/or post-processing methods such as polynomial fitting[33,34] or N4ITK bias correction.[35] Together with z-score signal intensity normalization, this assures standardized ZTE signal response across the imaging FOV without RF shading effects.

Bone segmentation and synthetic CT

The ZTE image quality obtained following bias correction and normalization is sufficient to enable bone segmentation. In a typical histogram distribution of ZTE signal, there are clear peaks for air and soft tissue, with an intervening broader bone peak. Air, tissue, and bone segmentations can be obtained via intensity thresholding (*i.e.* air < $threshold_{air\text{-}bone}$<bone<$threshold_{bone\text{-}tissue}$ < tissue) and morphologic operations to account for partial volume effects.[33,34,36,37] Bone signal intensities in ZTE and

Figure 2. PD-weighted ZTE (FOV = 30 cm, res = 1 mm, FA = 1 deg, BW =± 62.5 kHz, 2 min 11 s) acquired at 1.5 T using a head & neck coil array with standard/gridding reconstruction (top), DL-reconstruction (middle), inverted grayscale (bottom) and DL-derived synthetic CT and derived 3D bone rendering. BW, bandwidth; FOV, field of view; PD, proton density; ZTE, zero echo-time.

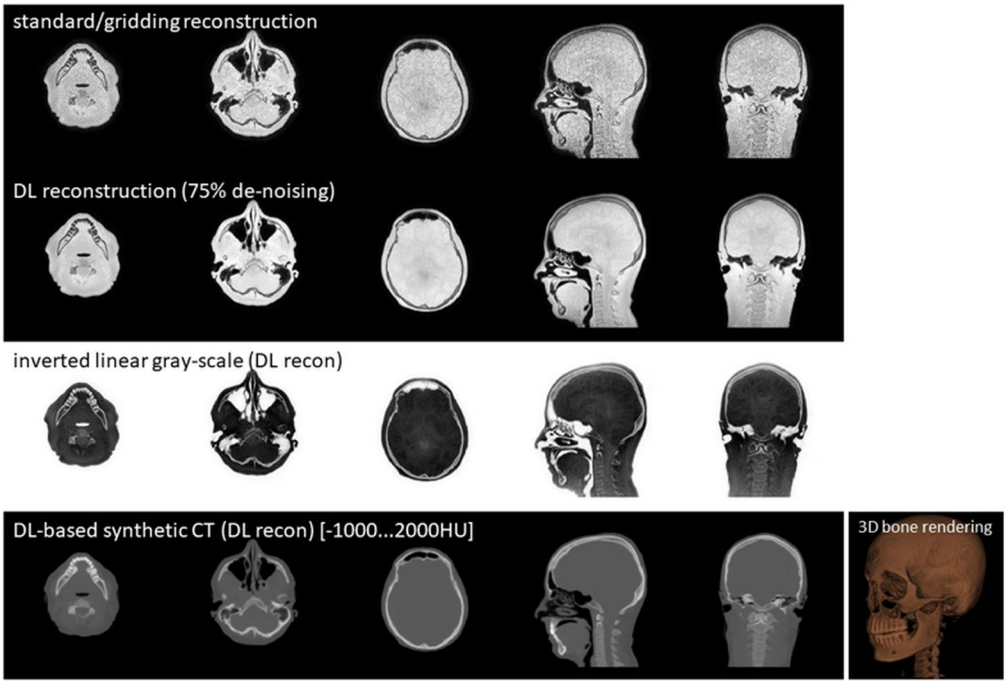

CT demonstrate a strong linear correction, such that robust segmentation and linear scaling (point-based operations) can generate synthetic CT images[34] for basic applications including MRI-only radiation treatment planning and PET/MRI attenuation correction[36,38–40] (Figure 3). With the advent of DL-based image segmentation and translation, more realistic synthetic CT images and 3D bone renderings can be created using convolutional neuronal networks (CNNs)[41–49] and generative adversarial networks (GAN).[50–53] For an excellent review on the subject of DL-based synthetic CT generation, we refer the interested reader to a recent ZTE review article.[44] So far, MRI-derived synthetic CTs have been used clinically in adult subjects with relatively normal bone anatomy. For more complex pathologies (poorly mineralized, thin, or irregular bone; variable soft tissues with similarly short-T2 properties), DL-powered synthetic CT approaches show promise but are not fully optimized for anatomic delineation given the current paucity of clinical training data.[54] Therefore, radiologists will benefit from routinely reviewing source ZTE images, which tend to be of higher quality and clinical diagnostic value in the head and neck (Figure 4).

Fat-water chemical shift artifacts

Due to 3D radial sampling, ZTE tissue uniformity and overall image quality can be severely affected by fat-water off-resonance. We illustrate examples of chemical shift artifacts in the pelvis at 3T in linear (top) and inverted (middle) grayscale. At the highest imaging bandwidth (BW = 250 kHz, left), soft tissue appears uniform and contrasts well against bone and air. However, at the lowest imaging bandwidth (BW = 62.5 kHz, right), there is severe chemical shift off-resonance artifact with signal interference at fat-water interfaces, severely degrading cortical bone depiction and overall image quality (Figure 5).

At 3T, the 3.5 ppm fat–water chemical shift translates into an off-resonance of Df ~440 Hz with an out-phase echo time of TE_{OP}~1.15 ms (at 1.5T, Df~220 Hz and TE_{OP}~2.3 ms). This causes signal dephasing along the 3D radial center-out spoke readout. More concretely, fat and water resonances are aligned (*i.e.* in-phase) at the start of the 3D radial spoke in the center of k-space immediately following RF excitation. During the readout, the fat and water signals disperse and accumulate a phase difference of $\Delta\varphi = \Delta f * T_{Read} = \Delta f * N_{Read} * \Delta t_{RX}$ until the end of the readout. Off-resonance effects increase with increasing B_0 field strength, decreasing bandwidth, and finer spatial resolution; and become apparent when the readout duration ($T_{read} = N_{read}{*}Dt_{Rx}$) extends beyond the out-phase echo time ($TE_{OP} = 1/(2{*}Df)$=1.15 ms at 3T and 2.3 ms at 1.5T). The associated chemical shift artifacts manifest with image blurring (of the off-resonant species) and signal interference at fat–water tissue interfaces, which severely affects the clarity of cortical bone depiction. Fat–water chemical shift artifacts can be minimized by changing imaging parameters (bandwidth, spatial resolution and B_0 field strength), and/or performing chemical shift decomposition-based in-phase reconstruction.[55] While fat/water suppression can be effective in eliminating off-resonance artifacts, it is less useful for ZTE bone imaging, due to the need for uniform soft-tissue signal.

Alternative bone imaging techniques

PD-weighted ZTE achieves excellent cortical bone depiction via: (1) efficient capture of short-lived bone signal and (2) uniform

Figure 3. Analytical ZTE to CT (and CT to ZTE) image translation (top). The 2D histogram distribution (bottom) illustrates a strong linear correlation between ZTE signal intensity and ZTE Hounsfield units. Reproduced with permission from reference.[34] ZTE, zero echo-time.

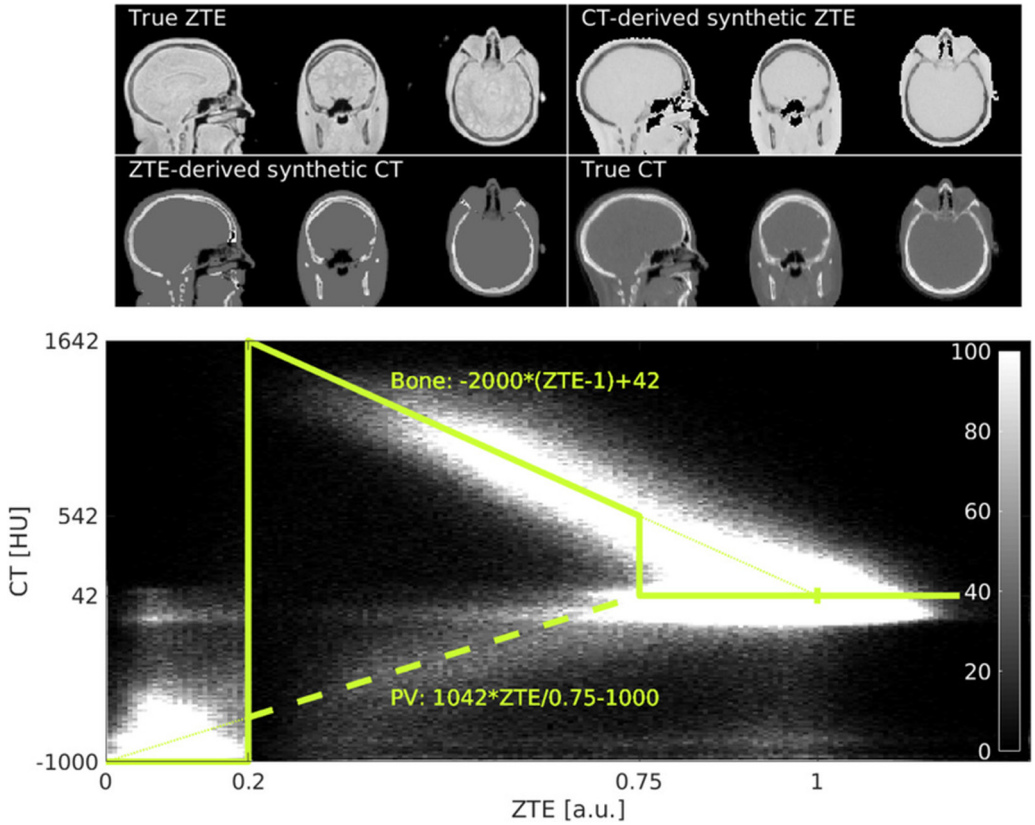

soft-tissue response. This method explores the unique strength of ZTE in terms of rapid, robust, 3D PD-weighted imaging.[33] ZTE can be combined with the traditional bone enhancement methods used in UTE imaging, including echo-subtraction[26] and magnetization prepared imaging.[56] These methods achieve selective bone depiction with true soft-tissue suppression, but involve significantly longer scan times and careful tuning of scan parameters and system performance (*i.e.* eddy current calibration). PD-weighted bone imaging can also be achieved with conventional gradient-echo (GRE) sequences, colloquially known as black bone MRI.[57] In this method, cortical bone appears dark (*i.e.* TE >> $T2_{bone}$) and more pronounced due to additional susceptibility effects at longer echo times.[58] However, there is a decreased ability to distinguish cortical bone from medullary bone and other short-T2 tissues. As an example, we compare bone depiction with PDw ZTE (top) *vs* PDw GRE (bottom), where the latter uses Dixon-type fat-water separation[59] to provide additional soft-tissue differentiation (Figure 6).

Clinical applications

Given its rapid, 3D, silent and artifact-resistant characteristics, ZTE is a viable alternative to CT for imaging cortical bone without ionizing radiation. In prior case series covering a variety of clinical applications, ZTE and CT show good diagnostic correlation among trained radiologists.[36,54,57,60–73] Current practical limitations of ZTE include inherently low SNR from weak bone signal, and limited spatial resolution of current MRI platforms (0.8–1 mm, compared to 0.5–0.6 mm with CT). It is likely that continued advances in MRI hardware and software will address these technical barriers, especially given that ZTE shows correlation with μCT for bone microstructure in *ex vivo* specimens.[74,75] With regard to image post-processing, synthetic CT algorithms are not fully ready for clinical prime-time, therefore experience in interpreting source ZTE images is important. Especially in the head and neck, complex anatomy and pathology can result in false-positives (other short-T2 tissues such as fibrous tissue, cartilage, inspissated secretions), as well as false-negatives (thin, unmineralized, irregular bone).

Based on the rapidity of ZTE, there is potential clinical utility for initial screening in the setting of acute trauma (evaluate for fractures and intracranial injury), abnormal head shape or size (evaluate for craniosynostosis and increased intracranial pressure), or bone abnormality (rule-out pathology). For more comprehensive examinations, ZTE can also be utilized to acquire bone information as part of a "one-stop-shop" MRI. This approach is particularly attractive in scenarios that would normally require both MRI and CT—*e.g.* craniofacial malformations, trauma, tumors, and interventional procedures. The advantages of a single MRI examination with ZTE—permitting combined soft tissue and bone characterization—could supersede the current workflow of sequential CT and MRI. The opportunity for longitudinal follow-up MRIs with ZTE are especially valuable to patients that require minimization or elimination of radiation exposure:

Figure 4. Synthetic CT generation using deep learning with encoder-decoder CNN architectures. (a) Example ZTE and CT images with synthetic CT generated using light U-Net (2,161,361 parameters), VGG-16 U-Net (28,845,505 parameters), and VGG-16 U-Net with TL from the ImageNet database. Bottom row shows color-coded subtraction maps of pixel-level differences between CT and synthetic CT. (b) Example ZTE and CT images with light U-Net using loss functions of MAE, MSE, and a weighted mixture of MAE and MSE. Models trained on MAE loss produce sharper-appearing synthetic CT images with fewer overall white pixels, resulting in better precision or positive predictive value for bone. Models trained on MSE loss produce smoother-appearing images with more overall white pixels, enabling better bone sensitivity or recall. The mixture loss provides a weighted average of the two contributions, balancing bone precision and recall. Courtesy of Sven Bambach, PhD. CNN, convolutional neural network; MAE, mean absolute error; MSE, mean squared error; TL, transfer learning; ZTE, zero echo-time.

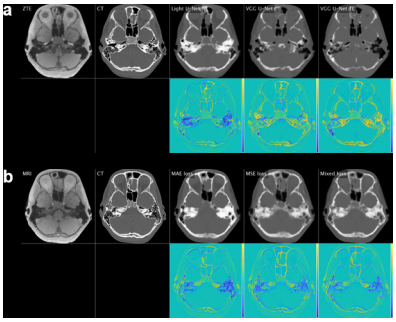

children, pregnant females, patients with cancer predisposition and related genetic syndromes, and chronic bone conditions requiring extended imaging surveillance.[37,60] Table 3 provides an overview of ZTE potential applications in the head and neck, organized by examination type, anatomic region, and disease process.

Craniofacial malformations

ZTE is useful for assessing craniofacial bony anatomy in the setting of abnormal head size, head shape, or dysmorphic facies suggestive of a genetic syndrome. The newborn skull consists of multiple flat bones separated by open sutures and fontanelles. Sutures are bridges of tough fibrous connective tissue that separate pairs of flat bones, while fontanelles are soft membrane-covered gaps located at the junctions of multiple cranial bones. These structures allow for plasticity of the cranial vault and enable passage through the birth canal. In the majority of infants, transient birth-related skull deformities will naturally correct over time. However, if a consistent external force is applied—usually from a stereotyped sleeping position—deformational or positional plagiocephaly results with asymmetric flattening of the skull. If the sutures remain open, there will be a compensatory asymmetric shift of the skull assuming a parallelogram morphology.[76–78] ZTE is a rapid, safe, and effective method to screen such infants, confirming the diagnosis of plagiocephaly with open sutures and normal intracranial pressures.[60]

Brain growth during childhood expands the cranial vault, keeps sutures open, and triggers additional osteogenesis. Monitoring head shape and circumference relative to age can aid in early diagnosis of pathology. Typical ages for fontanelle closure are: posterior 2–3 months, sphenoid 6 months, mastoid 6–18 months, anterior 9–18 months. Other than the metopic suture, which closes around 3–9 months of age, the remaining sutures (sagittal, coronal, lambdoid) normally stay open until brain growth ceases in the second decade. Premature closure of a suture is known as synostosis and can result from genetic or acquired (trauma, surgery, infection, malnutrition, brain injury) causes. The membranous bones actively remodel via central resorption and deposition of new bone along the periphery (suture edges). Therefore, the earliest manifestation of pathology will be narrowing of the involved suture (craniostenosis), followed by eventual closure (craniosynostosis).[79–82] On MRI, the fibrocartilaginous tissue within fontanelles and sutures has transverse relaxation time that is short, but slightly longer than ossified bone. Therefore on ZTE, the process of cranial ossification manifests with evolving PD signal, such that the relatively brighter fibrous gap gradually decreases in size and is ultimately replaced by a frank bony bridge.[37,79]

Isolated or single-suture synostosis accounts for the majority (at least 80%) of craniosynostosis cases. There is characteristic restriction of skull expansion perpendicular to the suture, with compensatory bone growth parallel and distal to the involved suture. This results in characteristic abnormal head shapes based on the affected sutures. Metopic synostosis presents with a "beak and notch" appearance (ectocranial ridging and endocranial notching), trigonocephaly (Greek for "triangle head"), and "quizzical eye" with elevation of the medial orbital rims. Sagittal synostosis is associated with dolichocephaly ("long head") or scaphocephaly ("boat head") when an overlying bony ridge is present. Coronal synostosis presents with anterior plagiocephaly, brachycephaly ("short head"), and a "harlequin eye" appearance with elevation of the superolateral orbit. Lambdoid synostosis presents with downward tilting of the back of head and a mastoid bulge behind the ear.[80,81]

Multisuture synostosis is far rarer, and usually genetic in etiology.[81] Turricephaly ("tower head") is seen with bilateral coronal and lambdoid synostosis; acrocephaly or oxycephaly ("point/sharp head") with coronal and sagittal synostosis; and Kleeblattschädel (German for "cloverleaf skull") with diffuse pancraniosynostosis. Additional craniofacial dysmorphisms can be characterized including frontal bossing, orbital changes, midface anomalies, skull base malformations, segmentation failures, facial clefts, micrognathia, and dental abnormalities. These abnormalities can be quantified using various metrics such as craniofacial and jaw ratios, orbital distances, and skull base measurements. Other craniofacial stigmata can also be assessed by ZTE, *e.g.* Luckenschädel ("lacunar") skull in Chiari II malformation; "bare orbit" and "asterion" signs in neurofibromatosis Type 1; "beaten brass" skull with increased intracranial pressure; dermal sinus tracts and inclusion cysts; and encephaloceles in various locations.[82] Finally, the brain develops concurrently with the face and is located in the same embryologic field, subject to similar molecular patterning and environmental influences—*i.e.* "the face predicts the brain".[66] Therefore, the use of MRI with ZTE is an excellent approach for comprehensively evaluating craniofacial and skeletal abnormalities—particularly if radiation needs to be avoided due to patient age (fetus, neonate, child) and/or status (pregnancy, cancer, radiation sensitivity).[37,61–66,79,83,84] (Figure 7)

Figure 5. ZTE fat–water chemical shift artifacts. Reproduced with permission from reference.[55] ZTE, zero echo-time.

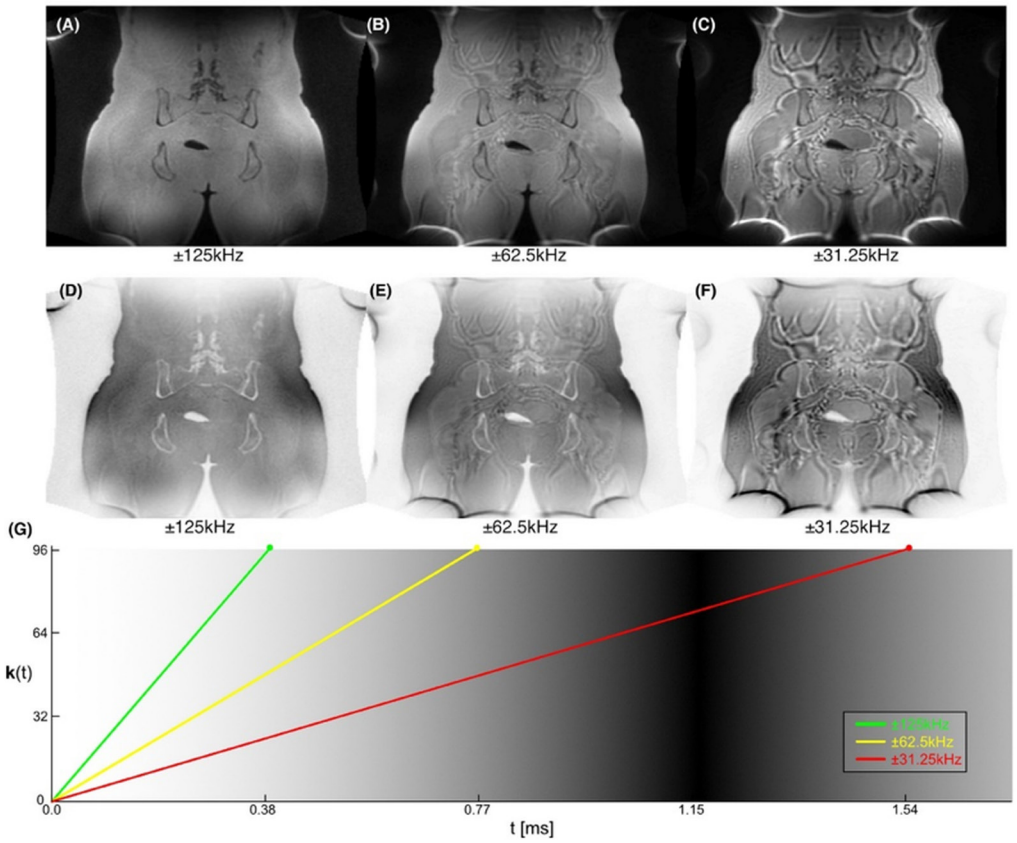

Trauma and stroke

Currently, CT is the accepted first-line modality for imaging of suspected stroke, trauma, and other acute neurologic conditions. This is a broadly utilized technique thanks to its rapid and accessible nature, with scanners available and easily operated at a variety of centers. Additionally, high-spatial resolution and attenuation-based technique are useful for evaluating hyperdense bone and hemorrhage. Nevertheless, MRI is becoming increasingly available and utilizes non-ionizing magnetic fields with multiple sequences providing high-contrast resolution.

Figure 6. Comparison of proton density-weighted ZTE (top) *vs* LAVA-Flex (bottom) bone depiction in the pelvis at 3T. ZTE, zero echo-time.

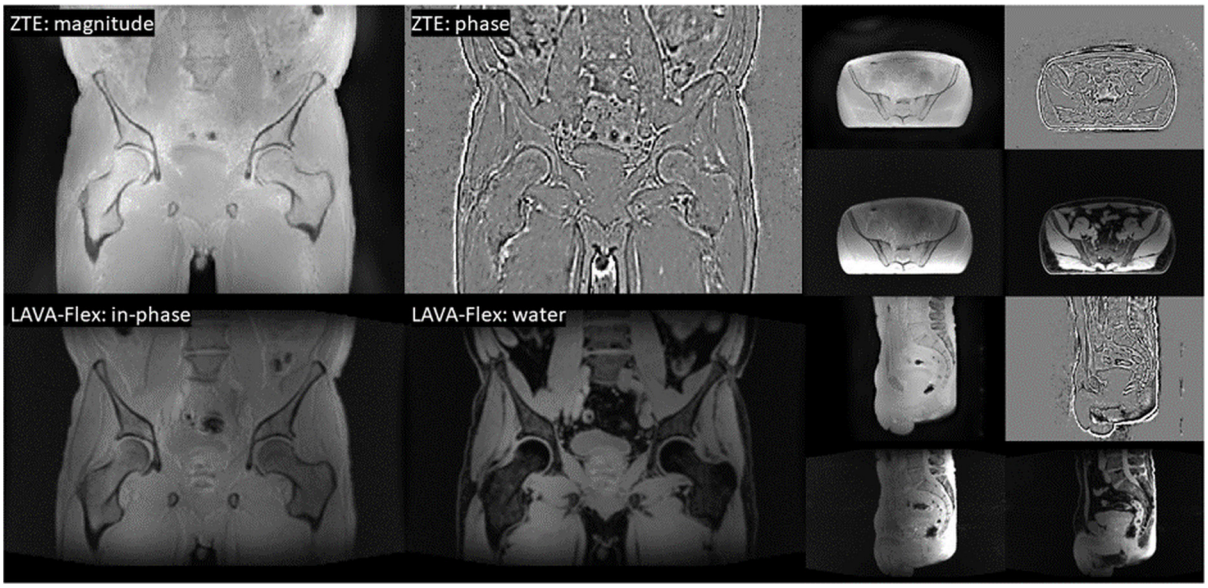

Table 3. ZTE clinical applications in the head and neck organized by examination type, anatomic region, and disease process

Examination type	Applications
Initial screening	Acute trauma Abnormal head shape or size Suspected bone abnormality
One-stop-shop MRI	Craniofacial malformations Stroke Trauma Tumors Infection and inflammation Follow-up examinations in patients with radiation sensitivity
Follow-up MRI	Children Pregnant females Genetic syndromes including cancer predisposition Chronic bone conditions
PET/MRI	Attenuation correction for PET Fully integrated imaging
Radiation therapy	Attenuation correction for dosimetry Multiparametric tissue mapping
Interventional radiology	Interventional planning Bone correction for ablation Intraoperative navigation and monitoring
Surgery	3D visualization and printing Surgical education and planning Intraoperative navigation Postoperative follow-up
Anatomic region	**Utility**
Cranial vault	Head shape Sutures and fontanelles Calvarial remodeling Encephaloceles
Skull base	Neurovascular canals and foramina Tumor, infection, inflammation
Face	Facial bones and orbit Dermal sinus tracts Sinonasal inflammation Tumors
Jaw	Jaw morphology and dentition Dental hardware Jaw tumors Osteomyelitis, osteonecrosis Temporomandibular joint
Disease process	**Diagnostic value**
Malformations	Plagiocephaly, single-suture, and multisuture craniosynostosis Congenital and acquired abnormalities of cranial vault, facial bones, skull base, and jaw
Trauma	Acute, healing, and chronic fractures Brain and soft tissue injury
Stroke	Intracranial calcification and hemorrhage Acute, subacute, and chronic infarcts
Tumor, infection, inflammation	Soft tissue components Marrow infiltration Cortical remodeling and breakthrough Periosteal reaction Pathologic fractures
Bone disorders	Mineralization status Joint inflammation, erosion, degeneration Bone morphology Pathologic fractures

PET, positron emission tomography; ZTE, zero echo-time.

Figure 7. Craniofacial malformations. (a) Left and right positional plagiocephaly. There is posterior flattening of the cranial vault with a parallelogram morphology. The coronal, squamosal, and lambdoid sutures are patent (arrows), demonstrating brighter signal than the ossified bone on proton density-weighted ZTE. In addition to bone, ZTE demonstrates brain parenchyma, ventricles, and subarachnoid spaces, and is a viable alternative to CT for rapid screening. (b) Metopic synostosis with triangular appearance of the anterior skull, ectocranial ridging (thick arrow) and endocranial notching (thin arrow) reflecting premature sutural fusion. (c) Right and left coronal synostosis (arrows) with anterior plagiocephaly and brachycephaly. (d) Apert syndrome with multisuture synostosis, turribrachycephaly, frontal bossing, midface hypoplasia, and skull base hypoplasia. The bilateral coronal, lambdoid, and sagittal sutures are prematurely fused (arrows). Mild ventriculomegaly is present with effaced peripheral subarachnoid spaces and gyral remodeling of the inner table ("beaten brass" appearance), suggesting increased intracranial pressure. (e) Achondroplasia with frontal bossing, macrocephaly, midface hypoplasia, J-shaped sella, narrow skull base, superiorly rotated petrous apices, medialized carotid canals, and foramen magnum stenosis. (f) Ecchordosis physaliphora (notochordal remnant) with T1-hypointense, T2-hyperintense and well-corticated osseous defect in the dorsal clivus (arrows). (g) Neurofibromatosis Type 1 with transspatial plexiform neurofibroma involving the left orbit, periorbital soft tissues, and temporal scalp. There is associated left buphthalmos and proptosis. ZTE shows expansion of the bony orbit and sphenoid wing dysplasia ("bare orbit" appearance). (h) Congenital midnasal stenosis with inward bowing of the nasal bones in the mid-nasal cavity (arrows), halfway between the pyriform apertures and choanae. (i) Congenital dermoid inclusion cysts overlying the frontonasal suture and right orbit (arrows). ZTE shows smooth subjacent osseous remodeling, without communicating intracranial tract. (j) Post-mortem imaging of infant with Meckel-Gruber syndrome showing microcephaly, overlapping sutures with occipital cephalocele (thick arrow), midface hypoplasia, and cleft palate (thin arrows). ZTE, zero echo-time.

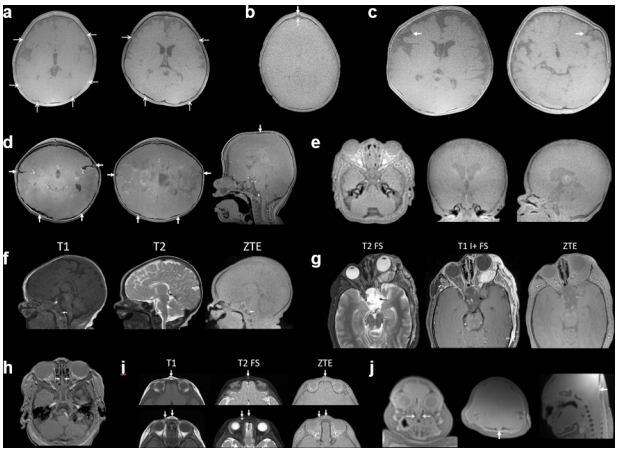

Rapid MRI protocols are being introduced in the acute neurologic setting, and can be even more sensitive than CT for specific applications, such as hyperacute stroke (with diffusion-weighted imaging), microhemorrhage and microcalcification

Figure 8. Trauma. (a) Comminuted and depressed right parieto-occipital skull fractures (arrows) with overlying subgaleal hematoma, underlying extra-axial hemorrhage, and brain hemorrhagic contusions. (b) Abusive head trauma with right greater than left subdural hematohygromas and bridging venous injury. ZTE shows diastatic sutures and bulging anterior fontanelle (arrow). (c) Right and left parietal growing fractures (leptomeningeal cysts), caused by dural injury with continued cerebrospinal fluid pulsations causing diastasis of the original skull fracture (arrows). (d) Organizing right parietal cephalohematoma with complex internal signal. On ZTE, there is early peripheral ossification (arrows) abutting the outer table. ZTE, zero echo-time.

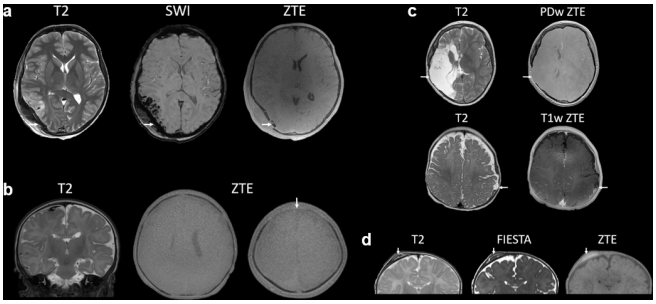

Figure 9. Chronic disorders. (a) Diffuse calvarial hyperostosis and pneumosinus dilatans in patient with chronic epilepsy on anticonvulsant therapy. (b) Arachnoid cysts (asterisks) of the right middle cranial fossa, left middle cranial fossa, and posterior fossa with associated parenchymal mass effect and smooth calvarial remodeling on ZTE. (c) Communicating hydrocephalus with severe tetraventricular enlargement, crowded subarachnoid spaces, and diastatic cranial sutures (arrows) on ZTE. (d) Chronic sinusitis with mucosal thickening, retention cysts, and maxillary sinus hyperostosis. (e) Giant cell lesion of the left mandibular angle (arrows). ZTE shows a multilobular expansile appearance with multiple curvilinear septations, cortical and alveolar erosions. (f) Desmoplastic fibroma arising from the right mandibular angle with heterogeneous exophytic soft tissue (arrows). ZTE demonstrates marrow expansion with alveolar erosions, lateral endosteal scalloping, medial cortical breakthrough, and aggressive periosteal reaction (sunburst and Codman triangle patterns). ZTE, zero echo-time.

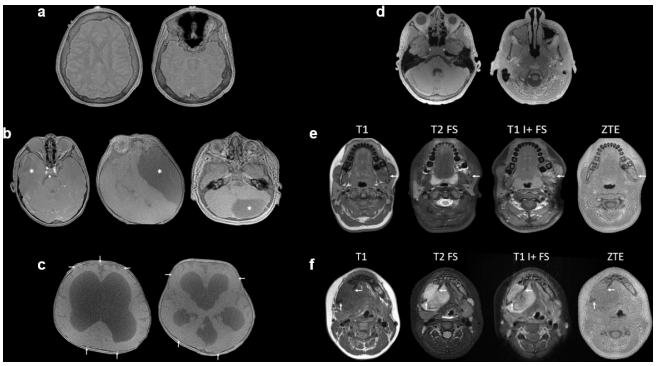

(using susceptibility-weighted imaging), and brain/soft tissue evaluation.[85–90]

In the setting of acute trauma, CT of the head and cervical spine are routinely ordered for rapid triage of fractures and hemorrhage. When CT findings, injury mechanism, and/or neurologic examination are concerning for brain or soft tissue injury, patients proceed to MRI. In hospitals with 24/7 MRI coverage, screening protocols are available for high-probability cases. As MRI becomes increasingly available in emergency departments, it is conceivable that a rapid MRI with ZTE could become an alternative first-line approach to imaging major trauma. Assuming no contraindications to MRI, the rapid readouts of ZTE also minimize susceptibility artifacts related to air and non-ferromagnetic foreign bodies. For patients with complex findings, such as traumatic brain injury or ligamentous injury, the rapid MRI could then be directly upgraded to a comprehensive "one-stop-shop" MRI at the radiologist's discretion.

In case series of acute trauma, ZTE successfully characterizes fractures of the cranial vault, facial bones, jaw, and spine.[68–73,79,90–92] As previously noted, standard MRI platforms provide slightly lower spatial resolution than CT, meaning that a non-displaced fracture or microfracture <1 mm could theoretically be missed using ZTE alone. However, most such fractures do not require intervention unless there is related brain or soft tissue injury, for which MRI is far more sensitive. With ongoing improvements in MRI hardware and software, ZTE will likely become able to delineate bone microstructure, based on *ex vivo* and animal studies with biomechanical and histopathological correlation.[74,75,93–97] In the subacute to chronic stage, MRI with ZTE is useful for evaluating healing *vs* non-healing fractures, organizing hematomas, and ossification[98,99] (Figure 8).

Tumors, infection, and inflammation

Bone is a dynamic organ that undergoes constant remodeling by osteoblasts, osteocytes, and osteoclasts.[100] Various pathologic conditions such as neoplasia, infection, and inflammation can yield characteristic patterns of bone remodeling visible on ZTE.[37,79,101] These patterns are related to the rate of progression, rather than histology. Aggressive bone lesions (*e.g.* osteomyelitis, fast-growing tumors) rapidly increase in size with imaging features including permeative bone destruction, soft tissue components, cortical breakthrough, florid periosteal reaction, and pathologic fractures. Non-aggressive lesions (*e.g.* slow-growing tumors) are indolent and produce well-defined geographic abnormalities with chronic bone remodeling and minimal smooth periostitis.[102]

ZTE provides excellent bony detail of the cranial vault and jaw. Cranial vault imaging is useful for evaluating calvarial remodeling secondary to various conditions including tumors, hydrocephalus, idiopathic intracranial hypertension, or chronic shunting.[37,79] In many countries, ZTE is routinely utilized in dentistry for evaluating tooth structure, jaw landmarks, and osseous remodeling. Given the superior soft tissue contrast and non-ionizing technique of MRI, this approach has clear advantages over CT in evaluating osteomyelitis, osteonecrosis, arthropathies. and suspected jaw tumors with associated marrow, pulp, and mucosal findings.[67,103,104] Due to the ultrafast readout of ZTE, dental amalgam and hardware demonstrate

Figure 10. Interventional procedures. (a) Shunted Chiari II with right plagiocephaly. ZTE shows the shunt catheter (arrows) with minimal susceptibility artifact. The ventricular system is mildly dilated with colpocephaly. The gyri are interdigitating due to hypoplasia of the interhemispheric falx. There is a Luckenschädel (lacunar) appearance of the skull. (b) Bithalamic high-grade glioma with enhancing and necrotic components, causing biventricular hydrocephalus and crowding of subarachnoid spaces. Postoperative ZTE shows nondependent pneumocephalus in the right frontal horn and shunt catheter in the third ventricle (arrow). (c) Post-surgical Shprintzen-Goldberg syndrome with pancraniosynostosis, turribrachycephaly, midface hypoplasia, and platybasia. ZTE shows surgical hardware, shunt reservoir (thick arrow), and catheter (thin arrows) with minimal susceptibility artifact. There is effacement of peripheral subarachnoid spaces and a "beaten brass" skull compatible with increased intracranial pressure. (d) Remote abusive head trauma with global parenchymal volume loss and chronic bilateral subdural hematomas with indwelling subdural shunts (arrows). Overshunting produces an "armored brain" appearance with diffuse calvarial hyperostosis. (e) Post-craniotomy for right parietal glioma resection (arrows). ZTE effectively distinguishes postoperative bone, metallic hardware, air, serous fluid, and hemorrhage, with minimal susceptibility artifacts. (f) Follow-up cranioplasty. ZTE shows polyetheretherketone implants and metal screws (arrows) with minimal susceptibility artifact. (g) Anterior cranial fossa reconstruction. Fixation plates and screws (arrows) show minimal susceptibility on ZTE. There is cystic encephalomalacia in both inferior frontal lobes. (h) Follow-up comminuted and depressed bifrontal calvarial fractures. Left frontal fixation plate and screws (arrows) show minimal susceptibility on ZTE. There is a left subdural hematoma and cystic encephalomalacia in the left greater than right inferior frontal lobes. (a) Repaired left zygomaticomaxillary fracture. Fixation plate and screws (arrows) show minimal susceptibility on ZTE. (i) Left segmental mandibulectomy follow-up. Residual mandibular bone (arrows) is well corticated, without concerning irregularity. The resection bed is filled with fat packing and there is no enhancing soft tissue to suggest recurrence. (j) Radiation therapy planning study for right skull base rhabdomyosarcoma (arrows) with infiltration of sphenoid bone and petrous apex, direct extension into middle cranial fossa, and perineural spread into pterygopalatine fossa, foramen rotundum, vidian canal, and foramen lacerum. ZTE demonstrates neoplastic bone erosions and osseous landmarks for radiation dosimetry. (k) Post-operative skull base chordoma. The resection bed is filled with fat packing material (arrows) and there is no enhancing soft tissue to suggest recurrence. ZTE demonstrates the transoral osseous resection defect. Pre- and post-contrast sequences depict cortical bone equally well, with enhancing marrow and vascular structures visible on the contrast study. ZTE, zero echo-time.

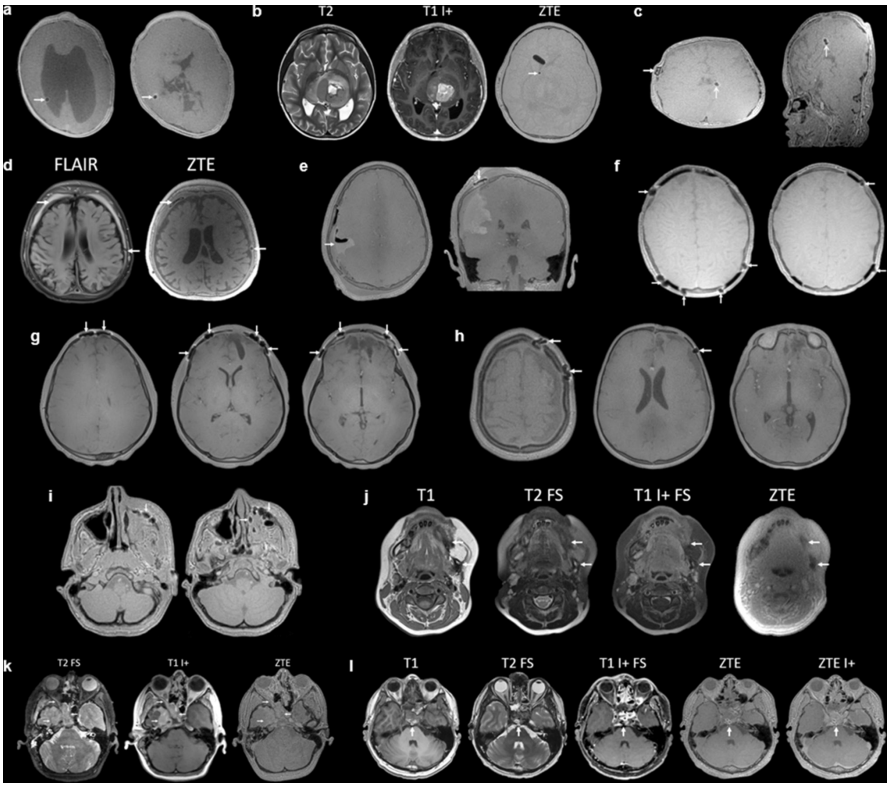

minimal susceptibility artifacts compared to conventional MRI sequences.[105–107]

ZTE of face and neck structures (orbits, sinonasal cavity, skull base, airway) is far more challenging than in the cranium and jaw. Factors that can degrade image quality include multiple bone–air interfaces, variable mucosal secretions, and complex soft tissue/fascial anatomy. These practical issues can be addressed by a combination of radiologist experience, improved sequence and post-processing tools. In patients requiring surveillance imaging examinations, "one-stop-shop" MRI with ZTE is a promising option tool for diagnosis, treatment planning, and longitudinal follow-up, offering higher contrast resolution and marginally lower spatial resolution than CT. This approach allows for integrated evaluation of cortical bone, bone marrow, and

soft tissues—ideal for complex pathologies that can demonstrate infiltrative involvement and perineural spread[37,54,79,108,109] (Figure 9).

Interventional procedures

Many medical interventions require perioperative image guidance prior to, during, and/or after the treatment session. Stereotactic approaches require precise 3D localization based on rigid nondeformable bony landmarks to perform various interventions such as biopsy, injection, stimulation, implantation, radiosurgery, ablation, or resection. In most clinical scenarios, CT and MRI examinations are acquired separately, then mathematically superimposed using various software packages. This approach leverages the bone detail and high spatial resolution of CT, along with the soft tissue contrast of MRI. However, patient motion during or between examinations can disrupt the image registration process and lead to incorrect spatial targeting. "One-stop-shop" MRI with ZTE—in which soft tissue and bone information are acquired in a single imaging session—offers several practical advantages for image-guided therapy. ZTE algorithms with computational corrections based on synthetic CT have been trialed for PET/MRI with attenuation correction, radiation therapy planning with dosimetry correction, and interventional ablation with skull correction.[34–53,110–113]

Perioperative surgical applications of ZTE are manifold. Many surgeons request 3D reconstruction, visualization, and/or printing to aid preoperative planning and intraoperative navigation. ZTE offers high-resolution, isotropic data sets with crisp bone detail and soft tissue contrast background suppression. However, typical 3D printing workflows are based on CT with intensity thresholding. This conventional pipeline is not well suited to identifying dark bone signal of ZTE, coexisting with multiple other short-T2 tissues against a brighter-intensity background. Therefore, ZTE bone segmentation in the head and neck can be fairly labor-intensive and requires knowledge of the underlying anatomy and pathology. In clinical patients, bone MRI with parameter optimization has been utilized to generate both physical 3D prints and virtual/augmented/mixed reality models.[37,54–57,64–66,68,108,109] Preliminary cadaver and surgical studies suggest that ZTE can be successfully used to plan operations on the cranium, jaw, face, skull base, and spine, with accuracy and outcomes comparable to CT.[114–119] Continued improvements in synthetic CT reconstruction approaches, as well as MRI hardware and software, should aid in greater adoption.

Within the surgical suite, intraoperative MRI units allow real-time image guidance and confirmation of procedural success without ionizing radiation exposure or follow-up imaging. During postoperative follow-up, hardware susceptibility is greatly reduced due to the ultrafast readout. ZTE incurs less artifacts when evaluating MRI-compatible needles, catheters, dental amalgam, ablation zones, and surgical hardware. The paramagnetic relaxivity effects of gadolinium are also minimized, such that ZTE can be performed both pre- and post-contrast with negligible effects on bone detail. Treatment changes can be assessed similar to or better than CT, with distinction of air, edema, hemorrhage, and calcification.[120–123]

Existing barriers to widespread implementation of ZTE include patient awareness and access; radiologist understanding; clinician perception of added value; inherent MRI hardware/software limitations; and synthetic CT post-processing algorithms.[37,54,79,108] As ZTE technology continues to improve, large-scale comparative effectiveness studies will help quantify the relative diagnostic value, therapeutic outcomes, and cost-effectiveness relative to CT (Figure 10).

CONCLUSION

ZTE MRI is a robust alternative to CT for imaging of cortical bone without the use of ionizing radiation. This technology offers the advantages of rapid examination times, silent scanning, and artifact resistance. Applications of ZTE in the head and neck have historically been limited by complex anatomy and pathology. In this article, we discuss the imaging physics of ZTE with optimal settings for bone imaging including acquisition, processing, segmentation, synthetic CT generation, and artifacts. We also review clinical utility in the head and neck with imaging examples including malformations, trauma, tumors, and interventional procedures. Widespread clinical adoption will be accelerated by technical and post-processing improvements, cost-effectiveness analysis, physician education, and patient advocacy.

ACKNOWLEDGMENTS

The authors would like to thank Dr Sven Bambach for his deep learning expertise, and Drs. Houchun Harry Hu, Mark Smith, Naoharu Kobayashi, Aiming Lu, and Judd Storrs for their physics support.

CONFLICTS OF INTEREST

F.W. is an employee of GE Healthcare. M.L.H. was principal investigator on the Siemens Healthineers / Radiological Society of North America Research Scholar Grant, Society for Pediatric Radiology Pilot Award, and American Society of Head and Neck Radiology William N. Hanafee Grant for grants related to the topic of this review article. She is also funded by NIBIB R01 EB029957, NIH R01 NS 041922, DOD Exploration-Hypothesis Development Award TS200051, and Italfarmaco: ImagingDMD Research Grant, as well as co-investigator on the Bayer Healthcare Radiology Medical Education Grant and CHEST Foundation Research Grant in Cystic Fibrosis, for work unrelated to this article

REFERENCES

1. Madio DP, Lowe IJ. Ultra-fast imaging using low flip angles and fids. *Magn Reson Med* 1995; **34**: 525–29. https://doi.org/10.1002/mrm.1910340407
2. Weiger M, Pruessmann KP. *Encyclopedia of Magnetic Resonance [Internet]*. Chichester, UK: John Wiley & Sons, Ltd; 2012., p.: emrstm1292 Available from: http://doi.wiley.com/10.1002/9780470034590.emrstm1292
3. Weiger M, Pruessmann KP. Short-T2 MRI: principles and recent advances. *Progress in*

Nuclear Magnetic Resonance Spectroscopy 2019; **114–115**: 237–70. https://doi.org/10.1016/j.pnmrs.2019.07.001
4. Ljungberg E, Damestani NL, Wood TC, Lythgoe DJ, Zelaya F, Williams SCR, et al. Silent zero TE MR neuroimaging: current state-of-the-art and future directions. *Prog Nucl Magn Reson Spectrosc* 2021; **123**: 73–93. https://doi.org/10.1016/j.pnmrs.2021.03.002
5. Alibek S, Vogel M, Sun W, Winkler D, Baker CA, Burke M, et al. Acoustic noise reduction in MRI using silent scan: an initial experience. *Diagn Interv Radiol* 2014; **20**: 360–63. https://doi.org/10.5152/dir.2014.13458
6. Grodzki DM, Jakob PM, Heismann B. Correcting slice selectivity in hard pulse sequences. *Journal of Magnetic Resonance* 2012; **214**: 61–67. https://doi.org/10.1016/j.jmr.2011.10.005
7. Cheng L, Magland JF, Seifert AC, Wehrli FW. Correction of excitation profile in zero echo time (ZTE) imaging using quadratic phase-modulated RF pulse excitation and iterative reconstruction. *IEEE Trans Med Imaging* 2014; **33**: 961–69. https://doi.org/10.1109/TMI.2014.2300500
8. Schieban K, Weiger M, Hennel F, Boss A, Pruessmann KP. ZTE imaging with enhanced flip angle using modulated excitation: ZTE imaging with modulated excitation. *Magn Reson Med* 2015; **74**: 684–93.
9. Ljungberg E, Wood T, Solana AB, Kolind S, Williams SCR, Wiesinger F, et al. Silent T 1 m$_a$pping using the variable flip angle meth$_o$d with B 1 correction. *Magn Reson Med* 2020; **84**: 813–24.
10. Froidevaux R, Weiger M, Pruessmann KP. Pulse encoding for ZTE imaging: RF excitation without dead-time penalty. *Magnetic Resonance in Med* 2021; **87**: 1360–74. https://doi.org/10.1002/mrm.29056
11. Jackson JI, Meyer CH, Nishimura DG, Macovski A. Selection of a convolution function for fourier inversion using gridding [computerised tomography application]. *IEEE Trans Med Imaging* 1991; **10**: 473–78. https://doi.org/10.1109/42.97598
12. Beatty PJ, Nishimura DG, Pauly JM. Rapid gridding reconstruction with a minimal oversampling ratio. *IEEE Trans Med Imaging* 2005; **24**: 799–808. https://doi.org/10.1109/TMI.2005.848376
13. Fessler JA. On NUFFT-based gridding for non-cartesian MRI. *J Magn Reson* 2007; **188**: 191–95. https://doi.org/10.1016/j.jmr.2007.06.012
14. Pruessmann KP, Weiger M, Börnert P, Boesiger P. Advances in sensitivity encoding with arbitrary k -space trajectories: SENSE with arbitrary k -space trajectories. *Magn Reson Med* 2001; **46**: 638–51.
15. Knoll F, Bredies K, Pock T, Stollberger R. Second order total generalized variation (TGV) for MRI. *Magn Reson Med* 2011; **65**: 480–91. https://doi.org/10.1002/mrm.22595
16. Lustig M, Donoho D, Pauly JM. Sparse MRI: the application of compressed sensing for rapid MR imaging. *Magn Reson Med* 2007; **58**: 1182–95. https://doi.org/10.1002/mrm.21391
17. Wood T, Ljungberg E, Wiesinger F. Radial interstices enable speedy low-volume imaging. *JOSS* 2021; **6**: 3500. https://doi.org/10.21105/joss.03500
18. Lebel RM. Performance characterization of a novel deep learning-based MR image reconstruction pipeline. Available from: http://arxiv.org/abs/2008.06559
19. Wiesinger F, McKinnon G, Kaushik S, Solana AB, Ljungberg E, Vogel M, et al. *3D Silent Parameter Mapping: Further refinements & quantitative assessment*. ISMRM; 2021, p.1828.
20. Haase A. Snapshot flash mri. applications to t1, t2, and chemical-shift imaging. *Magn Reson Med* 1990; **13**: 77–89. https://doi.org/10.1002/mrm.1910130109
21. Mugler JP, Brookeman JR. Three-dimensional magnetization-prepared rapid gradient-echo imaging (3D MP RAGE). *Magn Reson Med* 1990; **15**: 152–57. https://doi.org/10.1002/mrm.1910150117
22. Solana AB, Menini A, Sacolick LI, Hehn N, Wiesinger F. Quiet and distortion-free, whole brain BOLD fmri using t2 -prepared RUFIS. *Magn Reson Med* 2016; **75**: 1402–12. https://doi.org/10.1002/mrm.25658
23. Irie R, Suzuki M, Yamamoto M, Takano N, Suga Y, Hori M, et al. Assessing blood flow in an intracranial stent: A feasibility study of MR angiography using A silent scan after stent-assisted coil embolization for anterior circulation aneurysms. *AJNR Am J Neuroradiol* 2015; **36**: 967–70. https://doi.org/10.3174/ajnr.A4199
24. Wood TC, Damestani NL, Lawrence AJ, Ljungberg E, Barker GJ, Solana AB, et al. Silent myelin-weighted magnetic resonance imaging. *Wellcome Open Res* 2020; **5**: 74. https://doi.org/10.12688/wellcomeopenres.15845.2
25. Yuan J, Hu Y, Menini A, Sandino CM, Sandberg J, Sheth V, et al. Near-silent distortionless DWI using magnetization-prepared RUFIS. *Magn Reson Med* 2020; **84**: 170–81. https://doi.org/10.1002/mrm.28106
26. Lee HM, Weiger M, Giehr C, Froidevaux R, Brunner DO, Rösler MB, et al. Long-T_2 -suppressed zero echo time imaging with weighted echo subtraction and gradient error correction. *Magn Reson Med* 2020; **83**: 412–26. https://doi.org/10.1002/mrm.27925
27. Wiesinger F, Menini A, Solana AB. Looping star. *Magn Reson Med* 2019; **81**: 57–68. https://doi.org/10.1002/mrm.27440
28. Kuethe DO, Caprihan A, Lowe IJ, Madio DP, Gach HM. Transforming NMR data despite missing points. *J Magn Reson* 1999; **139**: 18–25. https://doi.org/10.1006/jmre.1999.1767
29. Grodzki DM, Jakob PM, Heismann B. Ultrashort echo time imaging using pointwise encoding time reduction with radial acquisition (PETRA). *Magn Reson Med* 2012; **67**: 510–18. https://doi.org/10.1002/mrm.23017
30. Wu Y, Dai G, Ackerman JL, Hrovat MI, Glimcher MJ, Snyder BD, et al. Water- and fat-suppressed proton projection MRI (WASPI) of rat femur bone. *Magn Reson Med* 2007; **57**: 554–67. https://doi.org/10.1002/mrm.21174
31. Froidevaux R, Weiger M, Rösler MB, Brunner DO, Pruessmann KP. HYFI: hybrid filling of the dead-time gap for faster zero echo time imaging. *NMR Biomed* 2021; **34**(6): e4493. https://doi.org/10.1002/nbm.4493
32. Du J, Carl M, Bydder M, Takahashi A, Chung CB, Bydder GM. Qualitative and quantitative ultrashort echo time (UTE) imaging of cortical bone. *J Magn Reson* 2010; **207**: 304–11. https://doi.org/10.1016/j.jmr.2010.09.013
33. Wiesinger F, Sacolick LI, Menini A, Kaushik SS, Ahn S, Veit-Haibach P, et al. Zero TEMR bone imaging in the head: zero TE bone imaging. *Magn Reson Med* 2016; **75**: 107–14.
34. Wiesinger F, Bylund M, Yang J, Kaushik S, Shanbhag D, Ahn S, et al. Zero TE-based pseudo-CT image conversion in the head and its application in PET/MR attenuation correction and MR-guided radiation therapy planning. *Magn Reson Med* 2018; **80**: 1440–51. https://doi.org/10.1002/mrm.27134
35. Tustison NJ, Avants BB, Cook PA, Zheng Y, Egan A, Yushkevich PA, et al. N4ITK: improved N3 bias correction. *IEEE Trans Med Imaging* 2010; **29**: 1310–20. https://doi.org/10.1109/TMI.2010.2046908
36. Delso G, Wiesinger F, Sacolick LI, Kaushik SS, Shanbhag DD, Hüllner M, et al. Clinical evaluation of zero-echo-time MR imaging for the segmentation of the skull. *J Nucl Med* 2015; **56**: 417–22. https://doi.org/10.2967/jnumed.114.149997

37. Lu A, Gorny KR, Ho M-L. Zero TE MRI for craniofacial bone imaging. *AJNR Am J Neuroradiol* 2019; **40**: 1562–66. https://doi.org/10.3174/ajnr.A6175
38. Khalifé M, Fernandez B, Jaubert O, Soussan M, Brulon V, Buvat I, et al. Subject-specific bone attenuation correction for brain PET/MR: can ZTE-MRI substitute CT scan accurately? *Phys Med Biol* 2017; **62**: 7814–32. https://doi.org/10.1088/1361-6560/aa8851
39. Yang J, Wiesinger F, Kaushik S, Shanbhag D, Hope TA, Larson PEZ, et al. Evaluation of sinus/edge-corrected zero-echo-time–based attenuation correction in brain PET/MRI. *J Nucl Med* 2017; **58**: 1873–79. https://doi.org/10.2967/jnumed.116.188268
40. Delso G, Kemp B, Kaushik S, Wiesinger F, Sekine T. Improving PET/MR brain quantitation with template-enhanced ZTE. *Neuroimage* 2018; **181**: 403–13. https://doi.org/10.1016/j.neuroimage.2018.07.029
41. Leynes AP, Yang J, Wiesinger F, Kaushik SS, Shanbhag DD, Seo Y, et al. Zero-echo-time and dixon deep pseudo-CT (zedd CT): direct generation of pseudo-CT images for pelvic PET/MRI attenuation correction using deep convolutional neural networks with multiparametric MRI. *J Nucl Med* 2018; **59**: 852–58. https://doi.org/10.2967/jnumed.117.198051
42. Blanc-Durand P, Khalife M, Sgard B, Kaushik S, Soret M, Tiss A, et al. Attenuation correction using 3D deep convolutional neural network for brain 18F-FDG PET/MR: comparison with atlas, ZTE and CT based attenuation correction. *PLoS One* 2019; **14**(10): e0223141. https://doi.org/10.1371/journal.pone.0223141
43. . Kaushik S, Bylund M, Cozzini C, Shanbhag D, Petit S, Wyatt J, et al. Region of Interest focused MRI to Synthetic CT Translation using Regression and Classification Multi-task Network. IEEE JBHI. 2022;
44. Spadea MF, Maspero M, Zaffino P, Seco J. Deep learning based synthetic-CT generation in radiotherapy and PET: A review. *Med Phys* 2021; **48**: 6537–66. https://doi.org/10.1002/mp.15150
45. Gong K, Yang J, Kim K, El Fakhri G, Seo Y, Li Q. Attenuation correction for brain PET imaging using deep neural network based on dixon and ZTE MR images. *Phys Med Biol* 2018; **63**(12): 125011. https://doi.org/10.1088/1361-6560/aac763
46. Nie D, Cao X, Gao Y, Wang L, Shen D. Estimating CT image from MRI data using 3D fully convolutional networks. *Deep Learn Data Label Med Appl* 2016; **2016**: 170–78.
47. Andreasen D, Van Leemput K, Hansen RH, Andersen JAL, Edmund JM. Patch-based generation of a pseudo CT from conventional MRI sequences for MRI-only radiotherapy of the brain. *Med Phys* 2015; **42**: 1596–1605. https://doi.org/10.1118/1.4914158
48. . Boukellouz W, Moussaoui A. Magnetic resonance-driven pseudo CT image using patch-based multi-modal feature extraction and ensemble learning with stacked generalization. Journal of King Saud University - Computer and Information Sciences, 2019.
49. Simonyan K, Zisserman A. Very deep convolutional networks for large-scale image recognition. 2014.
50. Wolterink JM, Dinkla AM, Savenije MHF, et al. MR to CT synthesis using unpaired data. In: *Simulation and Synthesis in Medical Imaging. SASHIMI 2017. Lecture Notes in Computer Science*. Cham: Springer; 2017.
51. Zhu J-Y, Park T, Isola P, Efros AA. Unpaired Image-to-Image Translation Using Cycle-Consistent Adversarial Networks. 2017 IEEE International Conference on Computer Vision (ICCV); Venice; 2017. https://doi.org/10.1109/ICCV.2017.244
52. Isola P, Zhu J-Y, Zhou T, Efros AA. Image-to-Image Translation with Conditional Adversarial Networks. 2017 IEEE Conference on Computer Vision and Pattern Recognition (CVPR); Honolulu, HI; 2017. https://doi.org/10.1109/CVPR.2017.632
53. Li W, Li Y, Qin W, Liang X, Xu J, Xiong J, et al. Magnetic resonance image (MRI) synthesis from brain computed tomography (CT) images based on deep learning methods for magnetic resonance (MR)-guided radiotherapy. *Quant Imaging Med Surg* 2020; **10**: 1223–36. https://doi.org/10.21037/qims-19-885
54. Bambach S, Ho ML. *Bone MRI: can it replace CT? 2nd Place AI Award, Artificial Intelligence Workshop*. American Society of Functional Neuroradiology; 2020.
55. Engström M, McKinnon G, Cozzini C, Wiesinger F. In-phase zero TE musculoskeletal imaging. *Magn Reson Med* 2019; **83**: 195–202. https://doi.org/10.1002/mrm.27928
56. Ma Y-J, Zhu Y, Lu X, Carl M, Chang EY, Du J. Short T_2 imaging using a 3D double adiabatic inversion recovery prepared ultrashort echo time cones (3D DIR-UTE-cones) sequence. *Magn Reson Med* 2018; **79**: 2555–63. https://doi.org/10.1002/mrm.26908
57. Eley KA, Watt-Smith SR, Sheerin F, Golding SJ. "Black bone" MRI: a potential alternative to CT with three-dimensional reconstruction of the craniofacial skeleton in the diagnosis of craniosynostosis. *Eur Radiol* 2014; **24**: 2417–26. https://doi.org/10.1007/s00330-014-3286-7
58. Dimov AV, Liu Z, Spincemaille P, Prince MR, Du J, Wang Y. Bone quantitative susceptibility mapping using a chemical species-specific R2* signal model with ultrashort and conventional echo data. *Magn Reson Med* 2018; **79**: 121–28. https://doi.org/10.1002/mrm.26648
59. Dixon WT. Simple proton spectroscopic imaging. *Radiology* 1984; **153**: 189–94. https://doi.org/10.1148/radiology.153.1.6089263
60. Kuusela L, Hukki A, Brandstack N, Autti T, Leikola J, Saarikko A. Use of black-bone MRI in the diagnosis of the patients with posterior plagiocephaly. *Childs Nerv Syst* 2018; **34**: 1383–89. https://doi.org/10.1007/s00381-018-3783-0
61. Tan AP. MRI protocol for craniosynostosis: replacing ionizing radiation-based CT. *AJR Am J Roentgenol* 2019; **213**: 1374–80. https://doi.org/10.2214/AJR.19.21746
62. Low XZ, Lim MC, Nga V, Sundar G, Tan AP. Clinical application of "black bone" imaging in paediatric craniofacial disorders. *Br J Radiol* 2021; **94**(1124): 20200061. https://doi.org/10.1259/bjr.20200061
63. Eley KA, Watt-Smith SR, Golding SJ. "Black bone" MRI: a potential alternative to CT when imaging the head and neck: report of eight clinical cases and review of the oxford experience. *Br J Radiol* 2012; **85**: 1457–64. https://doi.org/10.1259/bjr/16830245
64. Eley KA, Watt-Smith SR, Golding SJ. "Black bone" MRI: a novel imaging technique for 3D printing. *Dentomaxillofac Radiol* 2017; **46**(3): 20160407. https://doi.org/10.1259/dmfr.20160407
65. Eley KA, Watt-Smith SR, Golding SJ. Three-dimensional reconstruction of the craniofacial skeleton with gradient echo magnetic resonance imaging ("Black bone"): what is currently possible? *J Craniofac Surg* 2017; **28**: 463–67. https://doi.org/10.1097/SCS.0000000000003219
66. Eley KA, Delso G. Automated 3D MRI rendering of the craniofacial skeleton: using ZTE to drive the segmentation of black bone and FIESTA-C images. *Neuroradiology* 2021; **63**: 91–98. https://doi.org/10.1007/s00234-020-02508-7
67. Lee C, Jeon KJ, Han SS, Kim YH, Choi YJ, Lee A, et al. CT-like MRI using the zero-TE technique for osseous changes of the TMJ. *Dentomaxillofac Radiol* 2020; **49**(3): 20190272. https://doi.org/10.1259/dmfr.20190272

68. Kralik SF, Supakul N, Wu IC, Delso G, Radhakrishnan R, Ho CY, et al. Black bone MRI with 3D reconstruction for the detection of skull fractures in children with suspected abusive head trauma. *Neuroradiology* 2019; **61**: 81–87. https://doi.org/10.1007/s00234-018-2127-9
69. Wu H, Zhong Y, Nie Q, Chen W, Guo L, Yang X, et al. Feasibility of three-dimensional ultrashort echo time magnetic resonance imaging at 1.5 T for the diagnosis of skull fractures. *Eur Radiol* 2016; **26**: 138–46. https://doi.org/10.1007/s00330-015-3804-2
70. Dremmen MHG, Wagner MW, Bosemani T, Tekes A, Agostino D, Day E, et al. Does the addition of a "black bone" sequence to a fast multisequence trauma MR protocol allow MRI to replace CT after traumatic brain injury in children? *AJNR Am J Neuroradiol* 2017; **38**: 2187–92. https://doi.org/10.3174/ajnr.A5405
71. Cho SB, Baek HJ, Ryu KH, Choi BH, Moon JI, Kim TB, et al. Clinical feasibility of zero TE skull MRI in patients with head trauma in comparison with CT: A single-center study. *AJNR Am J Neuroradiol* 2019; **40**: 109–15.
72. Deininger-Czermak E, Villefort C, von Knebel Doeberitz N, Franckenberg S, Kälin P, Kenkel D, et al. Comparison of MR ultrashort echo time and optimized 3D-multiecho in-phase sequence to computed tomography for assessment of the osseous craniocervical junction. *J Magn Reson Imaging* 2021; **53**: 1029–39. https://doi.org/10.1002/jmri.27478
73. Schwaiger BJ, Schneider C, Kronthaler S, Gassert FT, Böhm C, Pfeiffer D, et al. CT-like images based on T1 spoiled gradient-echo and ultra-short echo time MRI sequences for the assessment of vertebral fractures and degenerative bone changes of the spine. *Eur Radiol* 2021; **31**: 4680–89. https://doi.org/10.1007/s00330-020-07597-9
74. Geiger D, Bae WC, Statum S, Du J, Chung CB. Quantitative 3D ultrashort time-to-echo (UTE) MRI and micro-CT (μCT) evaluation of the temporomandibular joint (TMJ) condylar morphology. *Skeletal Radiol* 2014; **43**: 19–25. https://doi.org/10.1007/s00256-013-1738-9
75. Wurnig MC, Calcagni M, Kenkel D, Vich M, Weiger M, Andreisek G, et al. Characterization of trabecular bone density with ultra-short echo-time MRI at 1.5, 3.0 and 7.0 T--comparison with micro-computed tomography. *NMR Biomed* 2014; **27**: 1159–66. https://doi.org/10.1002/nbm.3169
76. Kiesler J, Ricer R. The abnormal fontanel. *Am Fam Physician* 2003; **15**: 2547–52.
77. Jung BK, Yun IS. Diagnosis and treatment of positional plagiocephaly. *Arch Craniofac Surg* 2020; **21**: 80–86. https://doi.org/10.7181/acfs.2020.00059
78. Idriz S, Patel JH, Ameli Renani S, Allan R, Vlahos I. CT of normal developmental and variant anatomy of the pediatric skull: distinguishing trauma from normality. *Radiographics* 2015; **35**: 1585–1601. https://doi.org/10.1148/rg.2015140177
79. Kobayashi N, Bambach S, Ho ML. Ultrashort echo-time MR imaging of the pediatric head and neck. *Magn Reson Imaging Clin N Am* 2021; **29**: S1064-9689(21)00673-5: 583–93: . https://doi.org/10.1016/j.mric.2021.06.008
80. . Ho ML, Eisenberg R. Neuroradiology Signs. 1st ed. McGraw Hill / Medical; 2014.
81. Johnson D, Wilkie AOM. Craniosynostosis. *Eur J Hum Genet* 2011; **19**: 369–76. https://doi.org/10.1038/ejhg.2010.235
82. LaMantia AS. Why does the face predict the brain? neural crest induction, craniofacial morphogenesis, and neural circuit development. *Front Physiol* 2020; **11**: 610970. https://doi.org/10.3389/fphys.2020.610970
83. Robinson AJ, Blaser S, Vladimirov A, Drossman D, Chitayat D, Ryan G. Foetal "black bone" MRI: utility in assessment of the foetal spine. *Br J Radiol* 2015; **88**(1046): 20140496. https://doi.org/10.1259/bjr.20140496
84. Kirmi O, Lo SJ, Johnson D, Anslow P. Craniosynostosis: a radiological and surgical perspective. *Semin Ultrasound CT MR* 2009; **30**: 492–512. https://doi.org/10.1053/j.sult.2009.08.002
85. Zhang XH, Liang HM. Systematic review with network meta-analysis: diagnostic values of ultrasonography, computed tomography, and magnetic resonance imaging in patients with ischemic stroke. *Medicine (Baltimore)* 2019; **98**(30): e16360. https://doi.org/10.1097/MD.0000000000016360
86. De Jong G, Kannikeswaran N, DeLaroche A, Farooqi A, Sivaswamy L. Rapid sequence MRI protocol in the evaluation of pediatric brain attacks. *Pediatr Neurol* 2020; **107**: 77–83. https://doi.org/10.1016/j.pediatrneurol.2019.12.007
87. Ramgopal S, Karim SA, Subramanian S, Furtado AD, Marin JR. Rapid brain MRI protocols reduce head computerized tomography use in the pediatric emergency department. *BMC Pediatr* 2020; **20**(1): 14. https://doi.org/10.1186/s12887-020-1919-3
88. Wharton JD, Barry MM, Lee CA, Massey K, Ladner TR, Jordan LC. Pediatric acute stroke protocol implementation and utilization over 7 years. *J Pediatr* 2020; **220**: 214–20. https://doi.org/10.1016/j.jpeds.2020.01.067
89. Algethamy HM, Alzawahmah M, Young GB, Mirsattari SM. Added value of MRI over CT of the brain in intensive care unit patients. *Can J Neurol Sci* 2015; **42**: 324–32. https://doi.org/10.1017/cjn.2015.52
90. Lehto LJ, Sierra A, Corum CA, Zhang J, Idiyatullin D, Pitkänen A, et al. Detection of calcifications in vivo and ex vivo after brain injury in rat using SWIFT. *Neuroimage* 2012; **61**: 761–72. https://doi.org/10.1016/j.neuroimage.2012.03.002
91. Vázquez E, Delgado I, Sánchez-Montañez A, Fábrega A, Cano P, Martín N. Imaging abusive head trauma: why use both computed tomography and magnetic resonance imaging? *Pediatr Radiol* 2014; **44**: S589-603. https://doi.org/10.1007/s00247-014-3216-5
92. Berger RP, Furtado AD, Flom LL, Fromkin JB, Panigrahy A. Implementation of a brain injury screen MRI for infants at risk for abusive head trauma. *Pediatr Radiol* 2020; **50**: 75–82. https://doi.org/10.1007/s00247-019-04506-1
93. Jerban S, Ma Y, Nazaran A, Dorthe EW, Cory E, Carl M, et al. Detecting stress injury (fatigue fracture) in fibular cortical bone using quantitative ultrashort echo time-magnetization transfer (UTE-MT): an ex vivo study. *NMR Biomed* 2018; **31**(11): e3994. https://doi.org/10.1002/nbm.3994
94. Weiger M, Stampanoni M, Pruessmann KP. Direct depiction of bone microstructure using MRI with zero echo time. *Bone* 2013; **54**: 44–47. https://doi.org/10.1016/j.bone.2013.01.027
95. Jerban S, Ma Y, Wong JH, Nazaran A, Searleman A, Wan L, et al. Ultrashort echo time magnetic resonance imaging (UTE-MRI) of cortical bone correlates well with histomorphometric assessment of bone microstructure. *Bone* 2019; **123**: 8–17. https://doi.org/10.1016/j.bone.2019.03.013
96. Jerban S, Ma Y, Jang H, Namiranian B, Le N, Shirazian H, et al. Water proton density in human cortical bone obtained from ultrashort echo time (UTE) MRI predicts bone microstructural properties. *Magn Reson Imaging* 2020; **67**: 85–89. https://doi.org/10.1016/j.mri.2020.01.004
97. Deininger-Czermak E, Euler A, Franckenberg S, Finkenstaedt T, Villefort C, Gascho D, et al. Evaluation of ultrashort echo-time (UTE) and fast-field-echo (FRACTURE) sequences for skull bone visualization and FRACTURE detection - A postmortem study. *J Neuroradiol*

2022; **49**: 237–43. https://doi.org/10.1016/j.neurad.2021.11.001
98. Gho SM, Shin J, Kim MO, Kim DH. Simultaneous quantitative mapping of conductivity and susceptibility using a double-echo ultrashort echo time sequence: example using a hematoma evolution study. *Magn Reson Med* 2016; **76**: 214–21. https://doi.org/10.1002/mrm.25869
99. Park H, Nam IC, Baek HJ, Ryu KH, Cho E, Kim SS, et al. Chronic intradiploic organizing hematoma of the skull mimicking calvarial tumor diagnosed using zero TE MRI: A case report and review of literature. *Medicina (Kaunas)* 2020; **57**(1): 18. https://doi.org/10.3390/medicina57010018
100. Florencio-Silva R, Sasso GR da S, Sasso-Cerri E, Simões MJ, Cerri PS. Biology of bone tissue: structure, function, and factors that influence bone cells. *Biomed Res Int* 2015; **2015**: 421746. https://doi.org/10.1155/2015/421746
101. Sandberg JK, Young VA, Yuan J, Hargreaves BA, Wishah F, Vasanawala SS. Zero echo time pediatric musculoskeletal magnetic resonance imaging: initial experience. *Pediatr Radiol* 2021; **51**: 2549–60. https://doi.org/10.1007/s00247-021-05125-5
102. Al-Qassab S, Lalam R, Botchu R, Bazzocchi A. Imaging of pediatric bone tumors and tumor-like lesions. *Semin Musculoskelet Radiol* 2021; **25**: 57–67. https://doi.org/10.1055/s-0041-1723965
103. Weiger M, Pruessmann KP, Bracher A-K, Köhler S, Lehmann V, Wolfram U, et al. High-resolution ZTE imaging of human teeth. *NMR Biomed* 2012; **25**: 1144–51. https://doi.org/10.1002/nbm.2783
104. Demirturk Kocasarac H, Geha H, Gaalaas LR, Nixdorf DR. MRI for dental applications. *Dent Clin North Am* 2018; **62**: 467–80. https://doi.org/10.1016/j.cden.2018.03.006
105. Cortes ARG, Abdala-Junior R, Weber M, Arita ES, Ackerman JL. Influence of pulse sequence parameters at 1.5 T and 3.0 T on MRI artefacts produced by metal-ceramic restorations. *Dentomaxillofac Radiol* 2015; **44**(8): 20150136. https://doi.org/10.1259/dmfr.20150136
106. Hövener JB, Zwick S, Leupold J, et al. Dental MRI: imaging of soft and solid components without ionizing radiation. *J Magn Reson Imaging* 2012; **36**: 841–46. https://doi.org/10.1002/jmri.23712
107. Hilgenfeld T, Prager M, Heil A. PETRA, MSVAT-SPACE and SEMAC sequences for metal artefact reduction in dental MR imaging. *Eur Radiol* 2017; **27**: 5104–12. https://doi.org/10.1007/s00330-017-4901-1
108. Smith M, Bambach S, Selvaraj B, Ho ML. Zero-TE MRI: potential applications in the oral cavity and oropharynx. *Top Magn Reson Imaging* 2021; **30**: 105–15. https://doi.org/10.1097/RMR.0000000000000279
109. Kirsch CF, Ho ML. Advanced magnetic resonance imaging of the skull base. *Semin Ultrasound CT MR* 2021; **42**: 229–52. https://doi.org/10.1053/j.sult.2021.04.006
110. Miller GW, Eames M, Snell J, Aubry JF. Ultrashort echo-time MRI versus CT for skull aberration correction in MR-guided transcranial focused ultrasound: in vitro comparison on human calvaria. *Med Phys* 2015; **42**: 2223–33. https://doi.org/10.1118/1.4916656
111. Guo S, Zhuo J, Li G, Gandhi D, Dayan M, Fishman P, et al. Feasibility of ultrashort echo time images using full-wave acoustic and thermal modeling for transcranial MRI-guided focused ultrasound (tcmrgfus) planning. *Phys Med Biol* 2019; **64**(9): 095008. https://doi.org/10.1088/1361-6560/ab12f7
112. Caballero-Insaurriaga J, Rodríguez-Rojas R, Martínez-Fernández R, Del-Alamo M, Díaz-Jiménez L, Ávila M, et al. Zero TE MRI applications to transcranial MR-guided focused ultrasound: patient screening and treatment efficiency estimation. *J Magn Reson Imaging* 2019; **50**: 1583–92. https://doi.org/10.1002/jmri.26746
113. Tokuda J, Wang Q, Tuncali K, Seethamraju RT, Tempany CM, Schmidt EJ. Temperature-sensitive frozen-tissue imaging for cryoablation monitoring using STIR-UTE MRI. *Invest Radiol* 2020; **55**: 310–17. https://doi.org/10.1097/RLI.0000000000000642
114. Suchyta MA, Gibreel W, Hunt CH, Gorny KR, Bernstein MA, Mardini S. Using black bone magnetic resonance imaging in craniofacial virtual surgical planning: A comparative cadaver study. *Plast Reconstr Surg* 2018; **141**: 1459–70. https://doi.org/10.1097/PRS.0000000000004396
115. Lethaus B, Gruichev D, Gräfe D, Bartella AK, Hahnel S, Yovev T, et al. "Black bone": the new backbone in CAD/CAM-assisted craniosynostosis surgery? *Acta Neurochir (Wien)* 2021; **163**: 1735–41. https://doi.org/10.1007/s00701-020-04445-z
116. Hoving AM, Kraeima J, Schepers RH, Dijkstra H, Potze JH, Dorgelo B, et al. Optimisation of three-dimensional lower jaw resection margin planning using a novel black bone magnetic resonance imaging protocol. *PLoS One* 2018; **13**(4): e0196059. https://doi.org/10.1371/journal.pone.0196059
117. Kang Y, Hua C, Wu B, Zhou Z, Xu Y, Wu P, et al. Investigation of zero TE MR in preoperative planning in dentistry. *Magn Reson Imaging* 2018; **54**: 77–83. https://doi.org/10.1016/j.mri.2018.07.007
118. Manoliu A, Ho M, Nanz D, Dappa E, Boss A, Grodzki DM, et al. MR neurographic orthopantomogram: ultrashort echo-time imaging of mandibular bone and teeth complemented with high-resolution morphological and functional MR neurography. *J Magn Reson Imaging* 2016; **44**: 393–400. https://doi.org/10.1002/jmri.25178
119. Connor SEJ, Borri M, Pai I, Barnsley H. "Black bone" magnetic resonance imaging as a novel technique to aid the pre-operative planning of posterior tympanotomy for cochlear implantation. *Cochlear Implants Int* 2021; **22**: 35–41. https://doi.org/10.1080/14670100.2020.1823126
120. Smith KA, Carrino JA, Carrino J. MRI-guided interventions of the musculoskeletal system. *J Magn Reson Imaging* 2008; **27**: 339–46. https://doi.org/10.1002/jmri.21274
121. Himes NC, Chansakul T, Lee TC. Magnetic resonance imaging-guided spine interventions. *Magn Reson Imaging Clin N Am* 2015; **23**: 523–32. https://doi.org/10.1016/j.mric.2015.05.007
122. Hiwatashi A, Yoshiura T, Yamashita K, Kamano H, Honda H. Ultrashort te mri: usefulness after percutaneous vertebroplasty. *AJR Am J Roentgenol* 2010; **195**: W365-8. https://doi.org/10.2214/AJR.10.4361
123. Jolesz FA. Future perspectives for intraoperative MRI. *Neurosurg Clin N Am* 2005; **16**: 201–13. https://doi.org/10.1016/j.nec.2004.07.011